Journal of Solid State Chemistry 217 (2014) 1–8

Contents lists available at ScienceDirect

Journal of Solid State Chemistry

journal homepage: www.elsevier.com/locate/jssc

Structural analysis of highly porous γ-Al_2O_3

Louise Samain [a], Aleksander Jaworski [b], Mattias Edén [b], Danielle M. Ladd [c], Dong-Kyun Seo [c], F. Javier Garcia-Garcia [d], Ulrich Häussermann [a,*]

[a] Department of Materials and Environmental Chemistry, Stockholm University, S-10691 Stockholm, Sweden
[b] Department of Materials and Environmental Chemistry, Physical Chemistry Division, Stockholm University, S-10691 Stockholm, Sweden
[c] Department of Chemistry and Biochemistry, Arizona State University, Tempe, AZ 85287-1604, USA
[d] ICTS Centro Nacional de Microscopía Electrónica, Facultad CC. Químicas, Universidad Complutense de Madrid, Madrid E-28040, Spain

ARTICLE INFO

Article history:
Received 19 December 2013
Received in revised form
4 May 2014
Accepted 9 May 2014
Available online 16 May 2014

Keywords:
Gamma alumina
Porous materials
Crystal structure
PDF analysis

ABSTRACT

Two highly porous γ-aluminas, a commercial catalyst obtained from the calcination of boehmite and a highly mesoporous product obtained from amorphous aluminum (oxy)hydroxide via a sol–gel-based process were investigated by ^{27}Al nuclear magnetic resonance (NMR), transmission electron microscopy (TEM), and atomic pair distribution function (PDF) analysis of synchrotron powder diffraction data. NMR data showed for both materials a distribution of tetrahedrally and octahedrally coordinated Al at a 0.30:0.70 ratio, which is typical for γ-aluminas. TEM studies revealed that rod-shaped particles with about 5 nm in thickness are the building blocks of the porous structure in both materials. These particles often extend to a length of 50 nm in the commercial catalyst and are considerably shorter in the sol–gel-based material, which has a higher surface area. Refinement of PDFs revealed the presence of a ~1 nm scale local structure and the validity of a tetragonal average structure for both materials. This tetragonal average structure contains a substantial fraction of non-spinel octahedral Al atoms. It is argued that the presence of local structure is a general feature of γ-alumina, independent of precursor and synthesis conditions. The concentration of "non-spinel" Al atoms seems to correlate with surface properties, and increases with increasing pore size/surface area. This should have implications to the catalytic properties of porous γ-alumina.

1. Introduction

Among the various transition aluminas γ-alumina (γ-Al_2O_3) is a most important catalyst and catalyst support in the automotive and petroleum industries [1]. Its desired textural properties, such as surface area, pore volume, and pore-size distribution, and its acid/base characteristics are mainly owed to surface chemical composition, local microstructure, and phase composition [1a]. The microstructure and thermal/hydrothermal stability of the material strongly depend on the synthetic methods and conditions, and yet the structural elucidation has been challenging due to the chemical structure similarities of the transition aluminas [1b].

The structure of γ-Al_2O_3 is traditionally considered as a cubic defect spinel type in which the oxygen atoms are arranged in a cubic close packing and Al atoms occupy the octahedral and tetrahedral sites. In space group $Fd\bar{3}m$ this translates to oxygen being situated on position 32*e*, and Al atoms on sites 8*a* (tetrahedral site) and 16*d* (octahedral site). To satisfy the γ-Al_2O_3 stoichiometry, deviating from the chemical formula of a spinel, M_3O_4 (M=a metal or mixed metals), the Al atomic positions are not fully occupied. Vacancies distribute over both the tetrahedral and octahedral sites 8*a* and 16*d* (spinel sites); however, the work of Zhou and Snyder showed that it is important to consider that Al atoms can also be located in (lightly occupied) "non-spinel" positions [2]. The precise distribution of Al atoms (and vacancies) is controversial and seems to depend on the preparation conditions of γ-Al_2O_3. Further complications come about due to the fact that both a cubic structure [2,3] and its tetragonal distortion [4] are found for boehmite- or gibbsite-derived γ-Al_2O_3, while other studies have proposed the existence of only a tetragonal structure [5]. For example, tetragonal γ-Al_2O_3 obtained from highly crystalline boehmite was reported to be present between 450 and 750 °C, which was evidenced from neutron diffraction studies [6]. In contrast, when derived from amorphous precursors (e.g. from sol–gel synthesis) γ-Al_2O_3 appears to preferentially adopt the cubic structure [6,7].

Paglia et al. established a tetragonal structure model with $I4_1/amd$ space group symmetry for γ-Al_2O_3 derived from calcination of highly crystalline boehmite [7], which has been rigorously

* Corresponding author.
E-mail address: Ulrich.Haussermann@mmk.se.se (U. Häussermann).

http://dx.doi.org/10.1016/j.jssc.2014.05.004

validated in a recent pair distribution function (PDF) analysis of synchrotron powder diffraction data [8]. This model contains a significant fraction of octahedrally coordinated Al on the non-spinel (8*c*) position ("Tetragonal-8*c*" model). Moreover, in their PDF study Paglia et al. showed that the Tetragonal-8*c* model only accounts for the average structure of γ-Al_2O_3 and that there is a previously undetected 1 nm scale local structure. The local structure possesses an oxygen arrangement similar to the boehmite precursor and was explained in terms of stacking defects formed during the creation of γ-Al_2O_3. It is important to emphasize that PDF analysis [9] was essential for establishing this new view of the structural properties of γ-Al_2O_3.

Despite its success, structural studies based on the PDF analysis are still relatively rare for γ-Al_2O_3 materials, given the fact that structural properties can vary significantly by applied synthetic routes and conditions. For example, it is not yet certain whether the recently discovered local structure exists in γ-aluminas that are prepared through other synthetic routes. Depending on synthesis conditions, furthermore, γ-Al_2O_3 samples may contain significant amounts of other transition aluminas, such as γ*-boehmite and γ-boehmite [10]. An emergent and vast application area for PDF analysis is the study of active sites, adsorbed molecules, and eventually in situ monitoring of catalytic processes [11,12]. Herein we report the PDF analysis of two porous γ-Al_2O_3 materials: a commercial catalyst prepared from boehmite powder and a highly mesoporous γ-Al_2O_3 prepared by a sol–gel-based method [13,14]. The intention of this study is to look into potential structural differences between differently prepared porous γ-aluminas and to investigate whether the finding of local structure according to Ref. [8] may be generalized. In this respect the sol–gel-based, amorphous Al_2O_3 derived, material is especially interesting. Its preparation method circumvents supercritical drying processes typically applied for production of high-porosity metal oxide materials [14]. Both materials have considerably higher surface areas and open pore structures than that investigated in Ref. [8] and represent "practical" catalysts.

2. Experimental methods

The commercial γ-Al_2O_3 catalyst (from calcined boehmite, in the following denoted as COMM, was purchased from Alfa Aesar, a Johnson Matthey Company (Catalog no. 43832; aluminum oxide, gamma-phase, catalyst support, high surface area, and bimodal). Highly mesoporous γ-Al_2O_3 was synthesized using a modified nonalkoxide gel method using aluminum chloride as the precursor and propylene oxide as an acid scavenger [13]. The method then involves a combustion process which removes a high boiling point organic liquid from the gel pores [14]. The γ-Al_2O_3 product obtained after combustion and calcination at 700 °C has been termed "pyrogel" [14], and hereafter will be denoted as PYRO. The high-energy X-ray diffraction experiments were carried out at the beamline P02.1, at PETRA III (DESY), Hamburg. This beamline operates at a fixed energy of approximately 60 keV. The wavelength has been determined to be 0.20727(6) Å by using a LaB_6 NIST standard. The beam size is approximately 0.8 mm in diameter.

The γ-Al_2O_3 powders were inserted into glass capillaries of 0.7 mm in diameter and placed in front of the detector. For both samples, 30 2D diffraction images, each obtained through the accumulation of 20 frames with an exposure time of one second per frame, were collected with a PerkinElmer amorphous silicon area detector placed at 262 mm from the sample. The distance between the sample and the detector was determined with a LaB_6 NIST standard. The 2D diffraction images were then integrated into a linear scattering signal with the software Fit2D and averaged [15].

The PDFs were extracted by using the PDFgetX2 software [16]. The different steps of the PDF extraction include the subtraction of the scattering signal from the container, the correction for Compton scattering, absorption effects, and multiple scattering, and normalization to obtain the function $S(Q)$. Finally the pair distribution function, $G(r)$, is obtained by sine Fourier transform of the normalized scattering intensity, $F(Q)=Q[S(Q)-1]$, to a maximum Q-value, Q_{max}, of 19.0 $Å^{-1}$. Identical PDFs (within a scale factor) were obtained by using the recently released PDFgetX3 [17], which confirmed the adequacy of the PDF extraction procedure with PDFgetX2.

Magic-angle-spinning (MAS) ^{27}Al nuclear magnetic resonance (NMR) spectra were acquired at a magnetic field of 14.1 T (−156.4 MHz ^{27}Al Larmor frequency) with a Bruker Avance III spectrometer. Finely powdered samples were packed into 3.2 mm zirconia rotors and spun at 24.00 kHz. The data acquisition employed short radiofrequency (rf) pulses (9° flip angle) with a spin nutation frequency of 100 kHz. 8192 signal transients were accumulated with relaxation delays of 5 s and a 600 kHz spectral window. A 1 M $Al(NO_3)_3$(aq) solution was employed both for rf pulse calibrations and shift referencing. The relative populations of the AlO_4 and AlO_6 species were extracted by a constrained iterative fitting based on numerically exact simulations using the protocol of Stevensson and Edén [18]. For each unique ^{27}Al site, Czjzek [19] and Gaussian distributions were assumed for the quadrupolar products and isotropic chemical shifts, respectively. Further details about the iterative fitting procedure are given in Ref. [20].

Transmission electron microscopy (TEM) studies were carried out in a JEOL JEM-3000F operated at 300 kV. Powder samples were ultrasonically dispersed in butanol and one drop of the resulting suspensions was deposited onto copper grids coated with a thin holey amorphous carbon layer. Images were recorded with a slow scan CCD camera. The samples were strongly charged under the beam of electrons when working at high magnification. This problem was mitigated to some extent by selecting the particles that were in good contact with the amorphous carbon layer or in their neighborhood. All images were recorded by inserting the objective aperture corresponding to the maximum resolution of the microscope (~1.7 Å). Excluding reflections with d values shorter than ~1.7 Å strongly improves the contrast in the images. The improvement is at the expense of lost information from these reflections.

3. Results and discussion

3.1. Qualitative analysis

The two γ-alumina materials compared in this study are considered as mesoporous (commercial product (COMM)); average pore diameter=9 nm, BJH pore volume=0.8 cm^3/g) and highly mesoporous (pyrogel (PYRO)); average pore diameter=21 nm; BJH pore volume=2.0 cm^3/g). Table 1 lists the reported pore and surface properties of both materials.

Fig. 1(a) displays ^{27}Al MAS NMR spectra recorded from PYRO and COMM. Both samples reveal essentially identical NMR characteristics that accord well with previous reports [21–23]. The peak maxima around 68 and 9 ppm reflect Al in tetrahedral and octahedral coordination, respectively, whereas the "signal-tails" towards lower shifts originate from distributions of quadrupolar couplings, as typically observed from disordered structures.

Fig. 1(b) shows the results of deconvoluting the NMR spectrum from PYRO into two peak components associated with each of AlO_4 and AlO_6 groups, yielding relative populations of 0.30 and 0.70, respectively (uncertainty ±0.02). The quality of the fit was further improved by including additional peak components accounting for

Table 1
Surface properties of investagated γ-Al_2O_3 materials. Commercial material is the Alfa Aesar product #43832 (aluminum oxide, gamma-phase, catalyst support, high surface area, bimodal).

Sample	BET surface area (m^2/g)	BET surface area from micropores[a] (m^2/g)	BJH desorption average pore diameter[b] (nm)	BJH adsorption cumulative pore volume[c] (cm^3/g)
Pyrogel (PYRO)	340	35	21	2.0
Commercial (COMM)	250	24	9	0.8

Pyrogel material was prepared according to Ref. [14].

[a] BET = Brunauer–Emmett–Teller, by the use of *t*-plots with the Harkins–Jura model.

[b] BJH = Barrett–Joyner–Halenda, (total pore volume)/(surface area).

[c] From the pores with a pore width not larger than 150 nm.

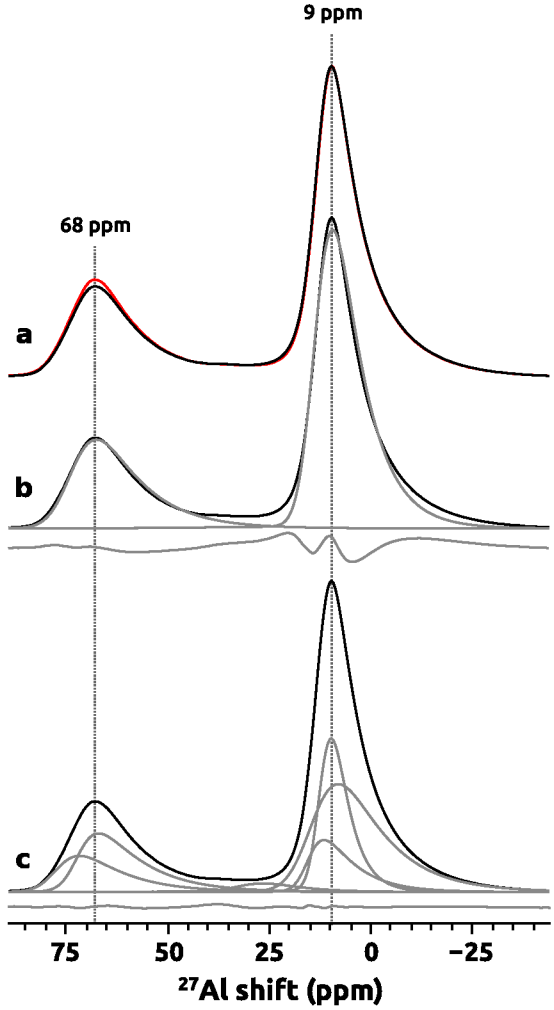

Fig. 1. (a) Experimental ^{27}Al MAS NMR spectra recorded from COMM (red trace) and PYRO (black trace), revealing resonances at 68 ppm and 9 ppm from AlO_4 and AlO_6 structural groups, respectively. (b) Deconvolution of the NMR spectrum from PYRO (black trace) into ^{27}Al signals from AlO_4 and AlO_6 groups (gray traces). The trace below the NMR spectrum represents the difference to its corresponding best-fit. (c) As in (b), but employing a total of six peak components. Note that both results of (b) and (c) provided the same relative AlO_4:AlO_6 populations of 0.30:0.70. (For interpretation of the references to color in this figure legend, the reader is referred to the web version of this article.)

the potential presence of non-equivalent sites of each primary (four/six) coordination, however, without any significant variations of the best-fit relative AlO_4:AlO_6 populations. Perander et al. [23] inferred the presence of minor AlO_5 populations by deconvoluting ^{27}Al MAS NMR spectra. By employing their six-peak deconvolution approach (see Fig. 1(c)), the AlO_4:AlO_5:AlO_6 populations relate as 0.287:0.025:0.688. However, we do not give any significance to the NMR parameters of this set of sites, other than noting that the AlO_4:AlO_6 populations relate as 0.30:0.70, in exact agreement with the result of the two-component fit of Fig. 1(b). High-resolution 3QMAS (triple-quantum MAS [24]) experiments did not reveal the presence of either AlO_5 species or of multiple AlO_4 or AlO_6 sites (data not shown). We conclude that if present, the contributions from AlO_5 groups must be very small (< 0.02).

Fig. 2 shows the diffraction patterns, reduced structure functions, $F(Q)$ and PDFs, $G(r)$ for both materials. The positions of the peaks in the PDF correspond to the separation of pairs of atoms, Al – Al, Al – O and O – O. Peaks below $r = 1.3$ Å result from termination ripples and do not correspond to any bond-length in the structure. The intensity of the peaks is related to the multiplicity of the atom-pairs (i.e., the number of atom-pairs at that particular distance) and is weighted by the scattering power of the atoms in the pair whereas their broadening depends on the distance distribution around the average bond-length value, which results from thermal vibrations or disorder.

Both the COMM and PYRO samples exhibit similar PDFs, which resemble those previously reported in the literature [8,11]. In order to make the comparison easier, the differential PDF (dPDF) is shown in Fig. 3, which was obtained by subtracting the PDF for PYRO from the one for COMM. Given the count statistics of the diffraction experiments, features larger than 0.12 $Å^{-2}$ can be considered as significant. Interatomic distances in both samples are virtually identical, with differences smaller than 0.01 Å. Slight intensity differences are observed between the PDFs, resulting in positive or negative features in the dPDF. This may indicate variations in the coordination environments in the samples, but a full interpretation of these differences would require refining the PDF based on a structural model.

Beyond 45 Å, no correlations are observed in both PDFs. The decrease in the PDF intensity indicates the presence of nano-domains of about 50 Å (5 nm). The instrumental resolution also influences the decrease in PDF intensity and is usually taken into account in the PDF refinement by a resolution damping factor determined from a standard. A previous study [11] has related this dampening factor to the particle size, and hence, to the surface area of the sample. Electron microscopy investigations (below) show that for both materials particle sizes are around 5 nm. For both PYRO and COMM, there is no evidence for inter-domain correlations from the PDFs. This suggests the absence of any kind of ordering among the pores at high r-range.

3.2. Electron microscopy investigations

Both samples display rather similar microstructures (Fig. 4) in which interconnected rod-like particles make up the three dimensional porous structure. In both samples, these rod-like particles have a similar thickness of around 5 nm, which agrees with the qualitative analysis of the PDFs, but they are different in length. (As a matter of fact, the thickness of the rods is also slightly different, as more clearly seen in the high resolution images and discussed below.) The nanorods in the COMM sample are typically at least 50 nm long, that is, more needle-shaped; in the PYRO sample they are considerably shorter.

Fig. 5 shows most representative high resolution images recorded for the COMM (Fig. 5a and b) and PYRO (Fig. 5c and d) samples. The alumina nanoparticles are in fact composed of very thin flakes which are stacked in a disordered manner. The thickness of the flakes was estimated to be 2–3 nm from the in-situ variation of the contrast with focus in the TEM. The images

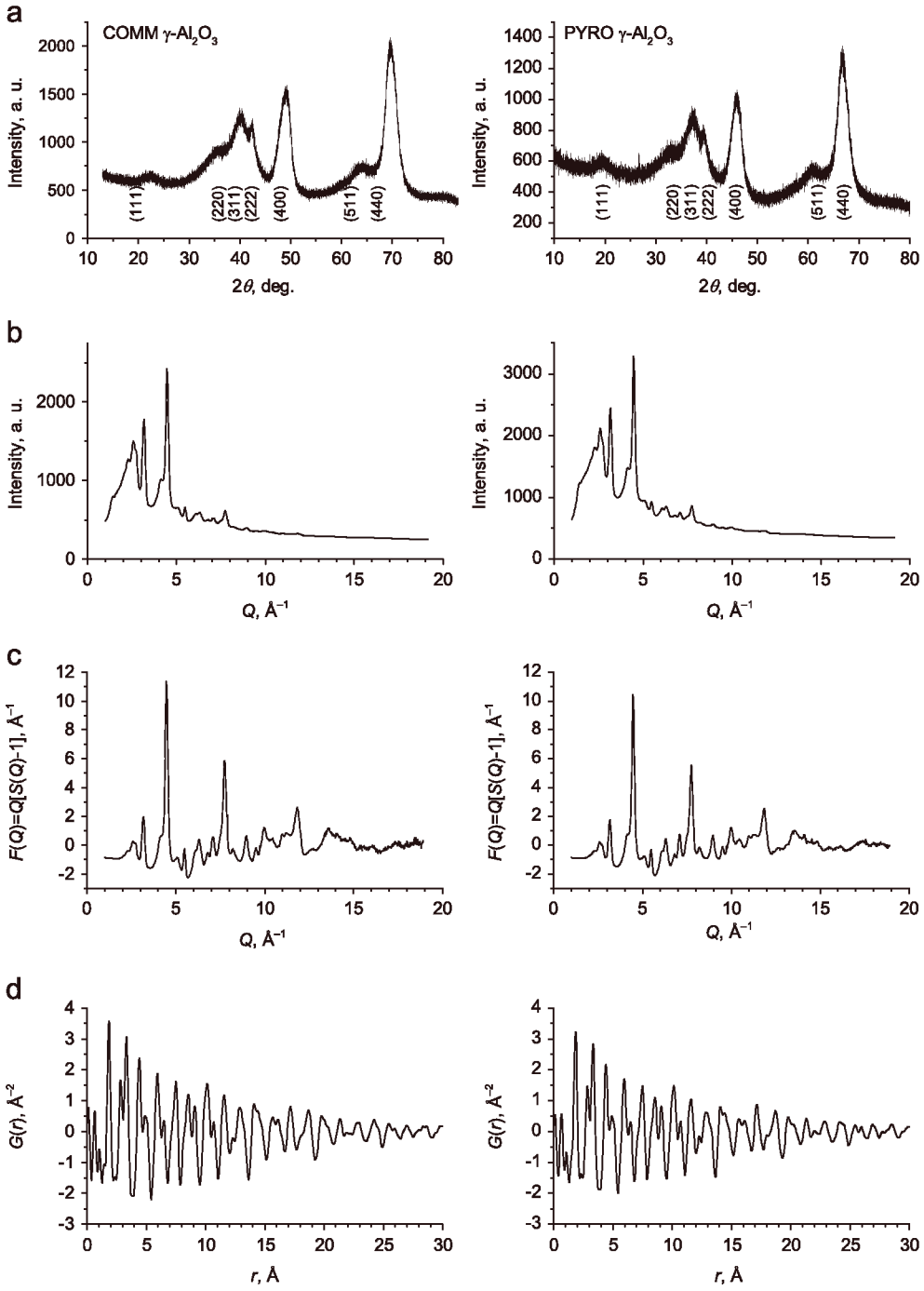

Fig. 2. Comparison of X-ray diffraction data for COMM (left hand panel) and PYRO samples (right hand panel). (a) Diffraction patterns obtained by using Cu-$K\alpha_1$ radiation ($\lambda = 1.5406$ Å), (b) High-energy diffraction patterns in Q-space ($\lambda = 0.2727$ Å), (c) the reduced structure function, $F(Q)$, and (d) the PDFs obtained by Fourier transforming $F(Q)$ shown above.

only show fringes as the flakes are randomly oriented with respect to the electron beam direction and thus the analysis has been carried out by using the corresponding digital diffraction patterns. The digital diffraction patterns show invariably and exclusively the 311 and 400 reflections ($d = 2.3$ and 1.9 Å, respectively). The 220 reflection was rarely observed, while the 111 did not appear at all. This agrees with the powder diffraction patterns of the samples where 311 and 400 are the most intense reflections whereas 220 and 111 are much weaker and diffuse (cf. Fig. 2a). The main difference discernible from the high resolution images was the shape of the flakes formed by the particles and not the structure within the flakes.

It is apparent that the rod-like particles building up the porous structure are different not only in length but also in thickness: particles of the PYRO sample are considerably shorter and also slightly thinner compared to those of the COMM sample (cf. Fig. 5b and d). In addition, PYRO particles possess a more globular shape (Fig. 5c). Furthermore, an interesting detail is noted on the extent of lattice fringes toward the boundary of flakes. In both samples the presence of amorphous domains is obvious, but locally there exist areas where fringes, and consequently the ordered atomic structure, extend to the very edge of a flake (stressed in Fig. 5 by rectangles). In essence, the COMM and PYRO samples differ slightly in terms of size and shape of the nanoparticles building

up the porous framework. This feature should be responsible for their different surface/pore properties shown in Table 1.

3.3. PDF refinement

The software PDFGui [9b] was used for PDF refinements which represent least square minimizations in the direct space of the experimental PDF with a periodic structural model. The structural model can be regarded as a bond-length distribution between all pairs of atoms i and j within the crystal, up to a maximum distance. Each contribution is weighted according to the product of the scattering factor of the atoms i and j. The Gaussian dampening factor, Q_{damp}, which accounts for the progressive decrease in the amplitude of the PDF peaks due to the limited Q-resolution, and the peak broadening from increased intensity noise at high Q, Q_{broad}, were determined from the PDF analysis of the LaB_6 standard to values of 0.068 and 0.001 $Å^{-1}$, respectively.

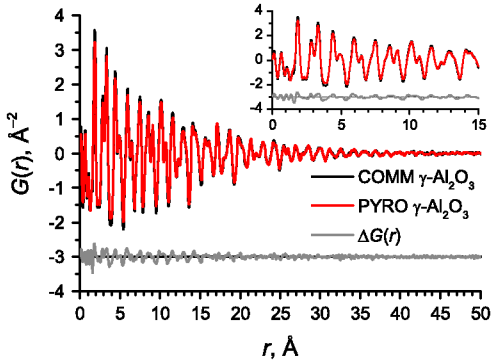

Fig. 3. PDFs for COMM and PYRO samples and their differential PDF.

In this work three models were tested to fit the PDF of γ-Al_2O_3, the conventional cubic spinel structure with $Fd\bar{3}m$ symmetry, but allowing partial occupancy of the non-spinel octahedral position 16*c* (Cubic-16*c* according to the nomenclature of Paglia et al. [7]), the tetragonal $I4_1/amd$ model with Al atoms only on (not fully occupied) spinel positions (4*a* and 8*d*) (termed Tetragonal-S hereafter), and the Tetragonal-8*c* model which in addition considers Al on the non-spinel octahedral position 8*c* (i.e., aforementioned Tetragonal-8*c*). The occupancy factors of Al sites were constrained to a total number of Al atoms of 21.333 and 10.667 in the unit cell of the cubic and tetragonal models, respectively, accounting for the overall chemical formula of alumina. For each model the scale factor and lattice parameters, and thermal parameters (coupled by symmetry constraints) were refined over a range of 1–20 Å. The results for COMM and PYRO were essentially identical, and only those for PYRO are shown in Fig. 6.

None of the proposed models resulted in a satisfactory refinement of the data, as indicated by the rather high weighed agreement factors R_{wp}. In particular the tetragonal models are inadequate to correctly describe the structure at short range, below 8 Å. For example the intensities of the peaks below 4 Å

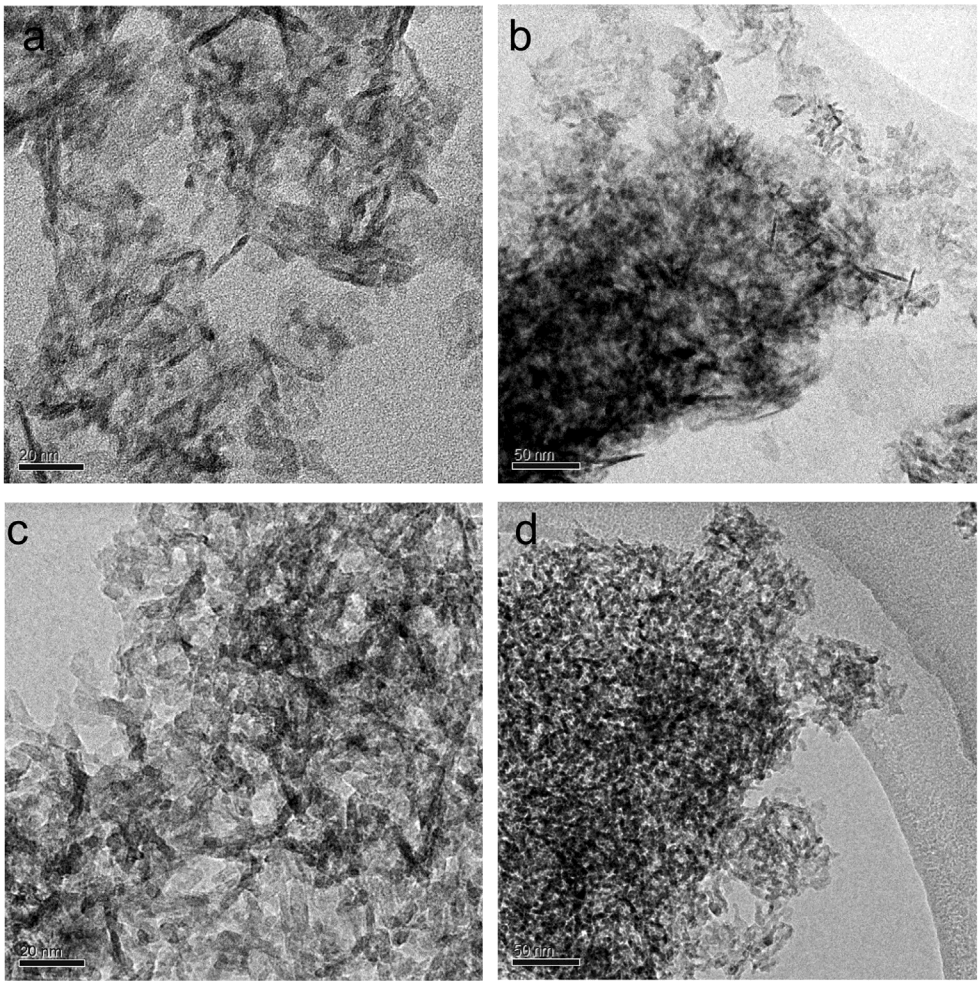

Fig. 4. Transmission electron microscopy images at intermediate magnifications of the COMM ((a) and (b)) and PYRO sample ((c) and (d)). Two magnifications are presented for each sample to account for differences at different spatial scale. Scale bar=20 nm for (a) and (c) and 50 nm for (b) and (d).

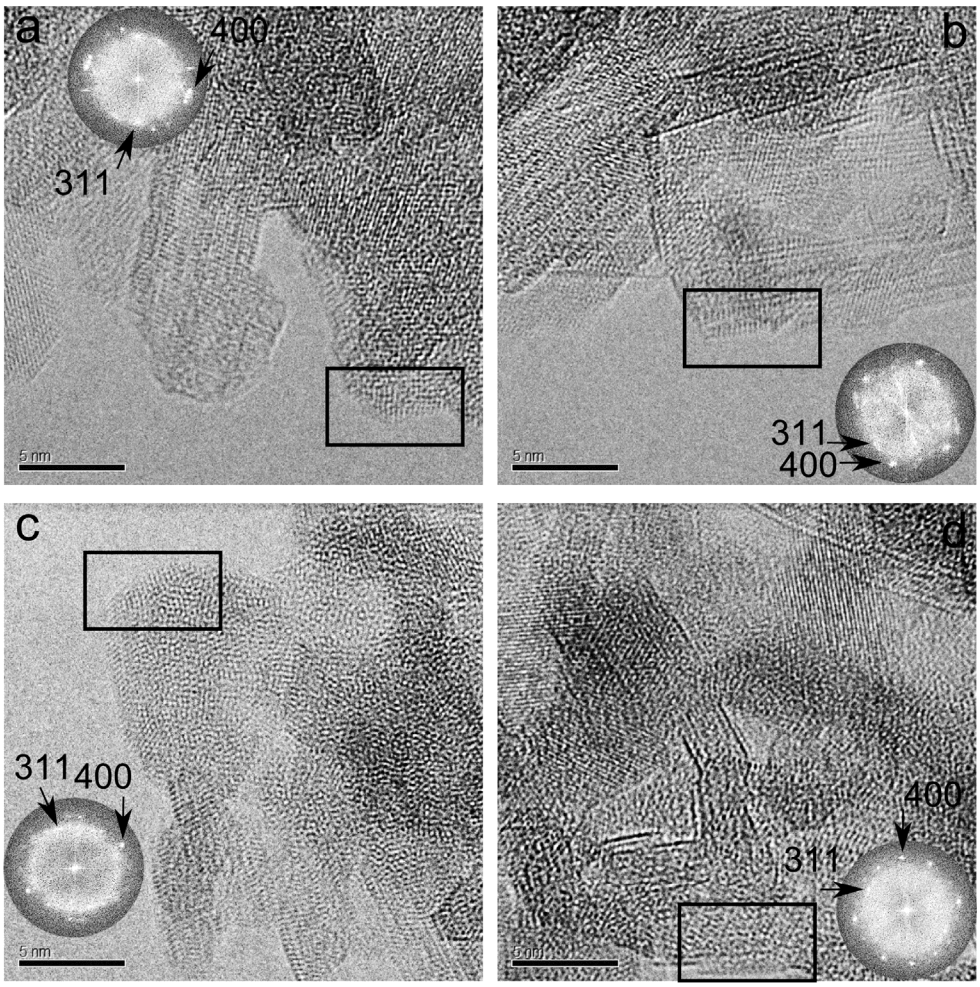

Fig. 5. Typical high resolution electron microscopy images recorded in the COMM sample, (a) and (b), and the PYRO sample, (c) and (d). Scale bar=5 nm. The digital difraction patterns are inserted and indexed. Alumina particles are composed of thin flakes that are stacked ramdonly. The most noticeable differences are observed in the size and shape of these flakes. The analysis of the fine contrast within the flakes render no differences between the both samples. Indicated areas show fringes extending to the very end of the flakes, see the text.

are strongly underestimated. Interestingly, the cubic model gives a slightly better R_{wp} (31.3% against 39.1% and 34.5% for the Tetragonal-S and the Tetragonal-8*c* model, respectively). Refinements of the atomic positions did not lead to a significant improvement of the fit for any of the three models.

When the fit range was set to 8 – 20 Å, however, the quality of the fit using the Cubic-16*c* and the Tetragonal-8*c* models was drastically improved (R_{wp}=20.5% and 20.1%, respectively, see Fig. 6, bottom). In contrast, the Tetragonal-S fails in describing the structure between 8 and 20 Å. The success of both Tetragonal-8*c* and Cubic-16*c* models can be attributed to the fact that Al is allowed to occupy non-spinel sites, in contrast with the Tetragonal-S model. However, upon comparing the refinement results for the Tetragonal-8*c* and Cubic-16*c* models, it appears that the oxygen thermal parameters in the Cubic-16*c* model are twice as large (0.030 Å^2 against 0.012 Å^2). The refinement of the oxygen atomic positions in the Cubic-16*c* model did not lead to an improvement of the fit nor a decrease of the O thermal factors, suggesting an increased disorder or a failure of the cubic model to adequately describe the oxygen atom distribution. The thermal parameters for Al for both models are comparable. Therefore one can conclude that the tetragonal models are more suitable than the cubic one in describing the average structure (> 8 Å) of the highly porous γ-Al_2O_3 materials, and that the Tetragonal-8*c* model works better than the Tetragonal-S model, as the former allows for the presence of non-spinel octahedrally coordinated Al. This observation contradicts the previous speculation that γ-Al_2O_3 derived from amorphous precursor exhibits a cubic structure [6,7]. Importantly, the tetragonal structure for a sol–gel-derived γ-Al_2O_3 has been recently reported for another highly porous material [11], although this material may have likely contained impurity phases, such as γ*-boehmite and γ-boehmite, due to the relatively low calcination temperature applied (400 °C).

The refined Tetragonal-8*c* average structure for PYRO and COMM displays only small differences. The lattice parameters for both samples, given in Table 2, are similar and are close to values previously reported in the literature [6,7]. The site occupancy factors (SOFs) for Al were allowed to vary, but constrained to match the relative AlO_4:AlO_6 population determined by the NMR experiments (0.30:0.70). The total number of Al atoms was constrained to 10.333 atoms, accounting for the Al_2O_3 composition. The refinement of Al occupancies, together with lattice and thermal parameters, led to a small improvement in the fit in the $8 < r < 20$ Å range, with a final R_{wp} of 19% for both samples. The obtained results for the Al SOFs are interesting (Table 2). Paglia et al. reported a spinel:non-spinel (8*d*:8*e*) ratio for octahedrally coordinated atoms as 36:58 for a material with a surface of 122 m^2/g [7]. For COMM and PYRO, however, we find 43:50 and 52:41 ratio, respectively, and it appears that the concentration of non-spinel Al increases with increasing surface area.

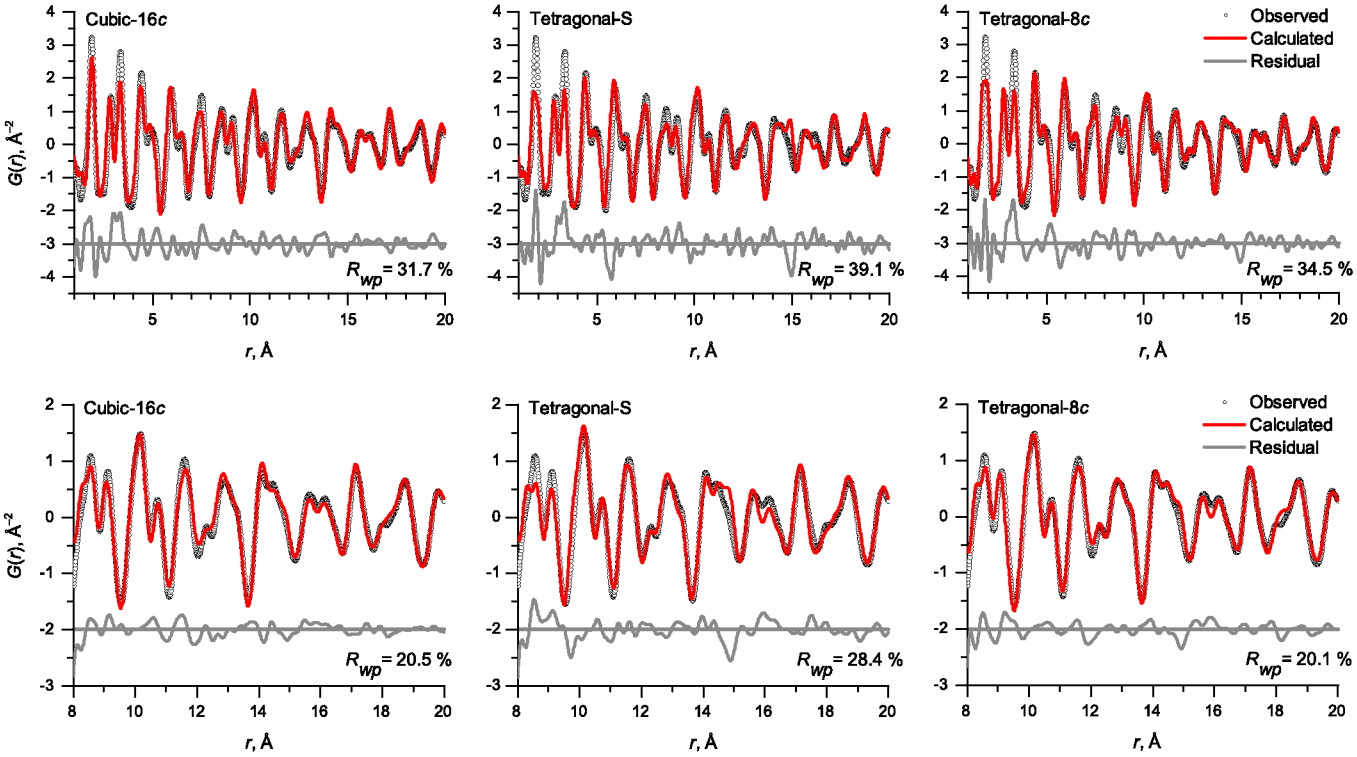

Fig. 6. Comparison between the observed PDF for PYRO and the calculated PDF for the Cubic-16*c*, Tetragonal-S, and Tetragonal-8*c* model over a fit range from 1 to 20 Å (top) and 8 to 20 Å (bottom).

Table 2
Lattice parameters and Al site occupancy factors for γ-Al_2O_3 with surface areas 122 m^2/g according to Paglia et al. [7], and 250 m^2/g (COMM) and 340 m^2/g (PYRO) obtained from PDF refinements using the Tetragonal-8*c* model for the average structure.

Site ($I4_1/amd$)	Paglia et al. [7] a=5.652(1) Å c=7.871(5) Å	Commercial γ-Al_2O_3 a=5.657(1) Å c=7.826(2) Å	Pyrogel γ-Al_2O_3 a=5.654(1) Å c=7.852(2) Å
4*a* (AlO_4)	0.78(2)	0.80	0.80
8*c* (AlO_6, non-spinel)	0.36(1)	0.43(3)	0.52(1)
8*d* (AlO_6)	0.58(1)	0.50(3)	0.41(1)
Total (AlO_6)	0.94(1)	0.933	0.933

For the COMM and PYRO refinements the AlO_4:AlO_6 population were constrained as 0.30:0.70 as obtained from the NMR investigation.

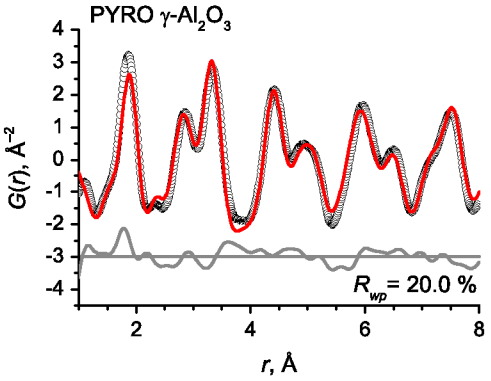

Fig. 7. Comparison between the observed PDF for PYRO from 1 to 8 Å and the calculated PDF for the local structure model reported by Paglia et al. [8].

As previously mentioned, the Tetragonal-8*c* model fails in modeling the observed PDFs in the low-*r* region (below 8 Å). Paglia et al. proposed that boehmite derived γ-Al_2O_3 consists of ~1 nm sized domains with a local structure different from the average one and provided a triclinic model that relates to the boehmite structure [8]. The tetragonal average structure at high *r*-range may then be reconciled as a superposition of different local defect structures, with stacking faults. We therefore tested the triclinic local structure model, containing 6 O and 4 Al atoms in an orthorhombic unit cell (according to Ref. [8]), on both COMM and PYRO. Only the scale factor and the thermal factors for Al and O (one per atomic species) were allowed to vary; the atomic positions were kept fixed to the values determined by Paglia et al. [8]. Experimental data and fit, shown in Fig. 7, are in a good agreement, although not as good as reported by Paglia et al. (R_{wp}=15.3%). For both γ-Al_2O_3 samples, the thermal factors for O and Al were refined to values that are 50% larger than those reported by Paglia et al. [8]. The intensity of the first peak at 1.8 Å

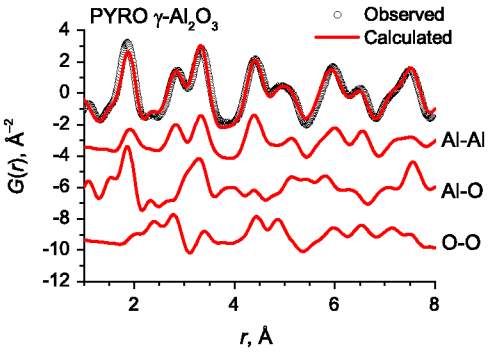

Fig. 8. Observed and refined PDFs for PYRO, and partial PDFs calculated for Al–Al, Al–O and O–O atomic pairs in the local structure model according to Paglia et al. [8].

is slightly underestimated. This peak corresponds to the shortest Al–O (1.86 Å) and Al–Al distances (1.92 Å), as shown by the partial PDFs, i.e., the PDFs calculated for each specific atom-pair in

the local structure, Al – Al, Al – O, and O – O (Fig. 8). Despite these discrepancies, it is clear that a ~1 nm scale local structure similar to the one reported by Paglia et al. [8] is also present in COMM and PYRO. Since Paglia et al.'s sample was derived from highly crystalline boehmite, it is reasonable to conclude that the presence and nature of the local structure do not depend on the precursors for the synthesis of γ-Al_2O_3, but rather is a general phenomenon.

4. Conclusions

Two highly porous γ-aluminas, a commercial catalyst obtained from the calcination of boehmite and a product obtained from amorphous precursor via a sol–gel-based process, were investigated by ^{27}Al NMR, TEM, and PDF analysis of synchrotron powder diffraction data. The distribution of tetrahedrally and octahedrally coordinated Al is 0.30:0.70 for both materials which is typical for γ-Al_2O_3. Furthermore, in both materials the porous structure is built up by rod-shaped particles with about 5 nm in thickness. These particles often reach 50 nm in length in the commercial catalyst and are considerably shorter in the sol–gel-based material. Both materials possess a ~1 nm scale local structure and a tetragonal average structure with a substantial fraction of octahedrally coordinated Al distributed over non-spinel sites. The presence of a local—possibly boehmite-related—structure may be a general feature of γ-alumina, independent of precursor and synthesis conditions. The concentration of "non-spinel" Al atoms increases with increasing pore size/surface area. This should have implications to the catalytic properties of porous γ-alumina.

Acknowledgments

This work was supported by the Swedish Research Council under Contract number 2011-6512 within the Ro ntgen-Ångstrom Cluster program. The work at ASU was supported by the Center for Bio-Inspired Solar Fuel Production, an Energy Frontier Research Center funded by the U.S. Department of Energy, Office of Science, Office of Basic Energy Sciences under Award number DE-SC0001016. M.E. acknowledges funding from the Swedish Research Council (2010-4943), the Faculty of Sciences at Stockholm University, and NMR equipment grants from the Swedish Research Council and the Knut and Alice Wallenberg Foundation. The authors acknowledge PETRA III, DESY, for provision of synchrotron radiation beamtime and thank Drs Hanns-Peter Liermann and Jozef Bednarcik for assistance in using beamline P02.1.

References

[1] (a) P. Euzen, P. Raybaud, X. Krokidis, H. Toulhoat, J.-L. Le Loarer, J.-P. Jolivet, C. Froidefond, in: F. Schüth, K.S.W. Sing, J. Weitkamp (Eds.), Alumina—Handbook of Porous Solids, Wiley-VCH Verlag GmbH, New York, 2002, pp. 1591–1677;
(b) M. Trueba, S.P. Trasatti, Eur. J. Inorg. Chem. 17 (2005) 3393–3403.
[2] R.S. Zhou, R.L. Snyder, Acta Crystallogr. B 47 (1991) 617–630.
[3] (a) K.P. Sinha, A.P.B. Sinha, J. Phys. Chem. 61 (1957) 758–761;
(b) Y.G. Wang, P.M. Bronsveld, J.T.M. DeHosson, B. Djuricic, D. McGarry, S. Pickering, J. Am. Ceram. Soc. 81 (1998) 1655–1660.
[4] (a) S.J. Wilson, J. Solid State Chem. 30 (1979) 247–255;
(b) S.J. Wilson, J.D.C. McConnell, J. Solid State Chem. 34 (1980) 315–322.
[5] T. Tsuchida, R. Furuichi, T. Ishii, Thermochim. Acta 39 (1980) 103–115.
[6] G. Paglia, C.E. Buckley, A.L. Rohl, R.D. Hart, K. Winter, A.J. Studer, B.A. Hunter, J. V. Hanna, Chem. Mater. 16 (2004) 220–236.
[7] G. Paglia, C.E. Buckley, A.L. Rohl, B.A. Hunter, R.D. Hart, J.V. Hanna, L.T. Byrne, Phys. Rev. B 68 (2003) 144110.
[8] G. Paglia, E.S. Bozin, S.J.L. Billinge, Chem. Mater. 18 (2006) 3242–3248.
[9] (a) T. Egami, S.J.L. Billinge, Underneath the Bragg Peaks: Structural Analysis of Complex Materials, Pergamon Press/Elsevier, Oxford, England (2003) 14;
(b) C.L. Farrow, P. Juhas, J.W. Liu, D. Bryndin, E.S. Bozin, J. Bloch, T. Proffen, S.J. T. Billinge, J. Phys.: Condens. Matter 19 (2007) 335219.
[10] J.A. Wang, X. Bokhimi, A. Morales, O. Novaro, T. Lopez, R. Gomez, J. Phys. Chem. B 103 (1999) 299–303.
[11] P.J. Chupas, K.W. Chapman, G.J. Halder, J. Am. Chem. Soc. 133 (2011) 8522–8524.
[12] L. Wei, R. Harrington, Y. Tang, J.D. Kubicki, M. Aryanpour, R.J. Reeder, J.B. Parise, B.L. Phillips, Environ. Sci. Technol. 45 (2011) 9687–9692.
[13] T.F. Baumann, A.E. Gash, S.C. Chinn, A.M. Sawvel, R.S. Maxwell, Chem. Mater. 17 (2005) 395–401.
[14] D.M. Ladd, A. Volosin, D.K. Seo, J. Mater. Chem. 20 (2010) 5923–5929.
[15] A.P. Hammersley, S.O. Svensson, M. Hanfland, A.N. Fitch, D. Häusermann, J. High Press. Res. 14 (1996) 235–248.
[16] X. Qiu, J.W. Thompson, S.J.L. Billinge, J. Appl. Crystallogr. 37 (2004) 678 (–678).
[17] (PDFgetX3) P. Juhás, T. Davis, C.L. Farrow, S.J.L. Billinge, J. Appl. Crystallogr. 46 (2013) 560–566.
[18] B. Stevensson, M. Edén, J. Chem. Phys. 134 (2011) 124104.
[19] G. Czjzek, J. Fink, F. Gotz, H. Schmidt, J.M.D. Coey, J.-P. Rebouillat, A. Liénard, Phys. Rev. B 23 (1981) 2513–2530.
[20] B. Pahari, S. Iftekhar, A. Jaworski, K. Okhotnikov, K. Jansson, B. Stevensson, J. Grins, M. Edén, J. Am. Ceram. Soc. 95 (2012) 2545–2553.
[21] D. Coster, A.L. Blumenfeld, J.J. Fripiat, J. Phys. Chem. 98 (1994) 6201–6211.
[22] M.-H. Lee, C.-F. Cheng, V. Heine, J. Klinowski, Chem. Phys. Lett. 265 (1997) 673–676.
[23] L.M. Perander, Z.D. Zujovic, T.F. Kemp, M.E. Smith, J.B. Metson, JOM - J. Min. Met. Mat. S 61 (11) (2009) 32–39.
[24] L. Frydman, J.S. Harwood, J. Am. Chem. Soc. 117 (1995) 5367–5368.